Pergamon

Acta mater. 49 (2001) 1909–1919

Acta MATERIALIA

www.elsevier.com/locate/actamat

NANOSCALE STRUCTURAL EVOLUTION OF Al_3Sc PRECIPITATES IN Al(Sc) ALLOYS

E. A. MARQUIS and D. N. SEIDMAN†

Department of Material Science and Engineering, 2225 North Campus Drive, Northwestern University, Evanston, IL 60208-3108, USA

(Received 12 November 2000; received in revised form 5 March 2001; accepted 7 March 2001)

Abstract—Precipitation of the Al_3Sc ($L1_2$) phase in aluminum alloys, containing 0.1, 0.2 or 0.3 wt% Sc, is studied with conventional transmission and high-resolution (HREM) electron microscopies. The exact morphologies of the Al_3Sc precipitates were determined for the first time by HREM, in Al–0.1 wt% Sc and Al–0.3 wt% Sc alloys. The experimentally determined equilibrium shape of the Al_3Sc precipitates, at 300°C and 0.3 wt% Sc, has 26 facets, which are the 6 {100} (cube), 12 {110} (rhombic dodecahedron), and 8 {111} (octahedron) planes, a Great Rhombicuboctahedron. This equilibrium morphology had been predicted by first principles calculations of the pertinent interfacial energies. The coarsening kinetics obey the $(\text{time})^{1/3}$ kinetic law of Lifshitz–Slyozov–Wagner theory and they yield an activation energy for diffusion, 164±9 kJ/mol, that is in agreement with the values obtained from tracer diffusion measurements of Sc in Al and first principles calculations, which implies diffusion-controlled coarsening.

Keywords: Aluminum; Scandium; Transmission electron microscopy (TEM); Phase transformations; Microstructure

1. INTRODUCTION

Dilute Al–Sc alloys [1] have excellent mechanical properties at room temperature, due to the presence of elastically hard and coherent Al_3Sc precipitates that can be obtained at a high number density [2–4]. These Al_3Sc precipitates remain coherent to a diameter of 20–30 nm, since the lattice parameter mismatch is 1.25% at room temperature [5]. The room-temperature strength of Al–Sc alloys is much higher than for any other alloying addition to Al on an atom-by-atom basis. The Al_3Sc phase is light (Sc is only 10% denser than Al) and it is extraordinarily stable (up to 1320±7°C) [6]. The Al_3Sc precipitates prevent recrystallization almost to the solidus by Zener pinning of grain boundaries, so that the strength of fine-grained Al–Sc alloys is low at elevated temperatures, because diffusional creep (or even superplasticity) occurs in a fine-grained structure [7]. It is therefore important to understand the microstructural behavior of this system for potential high temperature applications. The present study is part of a research program to correlate the microstructures of two-phase Al–Al_3Sc alloys with the high temperature creep properties of coarse-grained Al–Al_3Sc alloys for potential use for automotive and aerospace applications at elevated or ambient temperatures [8, 9].

The Al-rich primary solid-solution of the Al–Sc binary phase diagram exhibits a very narrow solid-solubility in equilibrium with the $L1_2$ Al_3Sc phase: see Fig. 1 [10, 11]. The maximum solid-solubility of Sc in Al, 0.38 wt% (0.21 at.%), occurs at the eutectic temperature (660.0–660.1°C). which is only 1°C below the melting point of pure aluminum. The eutectic composition is 0.47 wt% Sc (0.38 at.%). Decomposition of a supersaturated solid solution of Al(Sc) produces precipitation of the Al_3Sc phase, whose morphology depends on the aging temperature, the scandium concentration, and the aging time. Previous studies of Al alloys containing between 0.2 and 0.5 wt% Sc have shown that very fine, coherent and homogeneously distributed Al_3Sc precipitates with a 1.25% lattice parameter misfit at room temperature can be formed below 350°C [10, 12]. These precipitates are very stable with respect to coarsening, even for long aging times, and their size is in the range of 4–10 nm. Aging of an Al–0.5 wt% Sc alloy (hypereutectic composition) above 400°C results in rapid coarsening of the precipitates, which lose coherency when their size exceeds about 20–30 nm [13]. After loss of coherency, their shape is reported to be spherical [13].

† To whom all correspondence should be addressed. Tel: +1-847-491-4391; Fax: +1-847-467-2269.

E-mail address: d-seidman@northwestern.edu (D.N. Seidman)

1359-6454/01/$20.00
PII: S1359-6454(01)00116-1

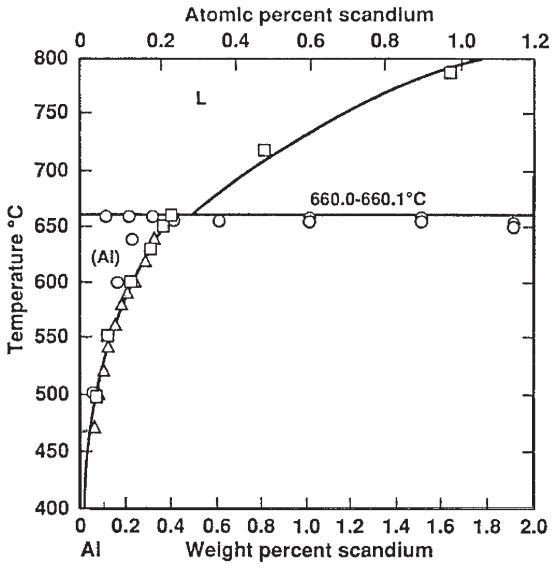

Fig. 1. The Al-rich side of the binary Al–Sc phase diagram [11].

The equilibrium shape of a coherent precipitate is determined by minimizing the sum of the interfacial and elastic energies at constant volume. The interfacial energy, which scales with the surface area of a precipitate, dominates the shape of the smaller precipitates. The elastic energy, due to the lattice mismatch accommodation across the coherent interface, scales with the volume of a precipitate and is dominant for larger-sized precipitates. Precipitates in aluminum alloys exhibit different shapes due to the anisotropy of the elastic constants and/or interfacial energies. For instance, platelets are observed in Al(Cu) alloys, and spheres in Al(Li) and Al(Zr) alloys; cubic precipitates, however, have not yet been reported in aluminum alloys, except for the study on Al(Sc) by Novotny and Ardell [14].

The Al–Sc system can also be compared to the well-studied Ni–Al system, as the phases have similar crystallographic structures. In both systems, the matrix is FCC and the precipitates have the $L1_2$ structure. The coarsening sequence of the Ni–Al system has undergone extensive observations showing that the Ni_3Al precipitate morphology evolves from spheres, to cubes, to arrays of cubes, to octets splitting into smaller precipitates [15–17]. Different attempts to model the strain energy effect reproduced the spherical to cubic shape evolution and predicted splitting of precipitates [18–20]. In the Ni–Al system, it is now well established that the morphology of the precipitates depends on the elastic strain self-energy and elastic interactions among precipitates, because of the high volume fraction of the Ni_3Al phase. The Al(Sc) system is interesting because the volume fraction of Al_3Sc precipitates, compared to the Ni–Al alloys, is small, but the elastic mismatch is fairly important. The effects of elastic interactions among precipitates should, therefore, be negligible in the Al–Sc system, while the elastic strain energy may play a role in the shape evolution of the Al_3Sc precipitates.

A recent CTEM study, investigating the effect of precipitate volume fraction on the coarsening kinetics, showed that, at low scandium concentration (0.2 wt% or 0.12 at.%), the Al_3Sc precipitates are cauliflower-shaped and evolve to spheres for long aging times at 350°C [14]. Studies of the Al–Li system have shown a significant effect of the supersaturation on the Al_3Li precipitate morphology and evolution [21]. For low supersaturations, growth instabilities develop resulting in non-spherical morphologies.

A more detailed study of the precipitation of the Al_3Sc phase should address the following questions. What is the exact shape of the smaller 5–10 nm Al_3Sc precipitates? How does the precipitate morphology evolve with time and temperature? What is the effect of Sc concentration on the precipitate morphology? What are the influences of temperature and Sc supersaturation on precipitation?

This article presents a study of the nanoscale structural evolution of small Al_3Sc precipitates in three aluminum alloys containing 0.1, 0.2 or 0.3 wt% Sc (0.06, 0.12, 0.18 at.%) in the temperature range 300–450°C. Our results contribute to an understanding of the governing mechanisms for the evolution of the Al_3Sc morphology during coarsening. HREM observations on Al_3Sc precipitates clarify the respective roles of the elastic strain and interfacial energies for small precipitate sizes.

2. EXPERIMENTAL PROCEDURES

The Al–0.1 wt% Sc, Al–0.2 wt% Sc, and Al–0.3 wt% Sc alloys are prepared by casting, using two master alloys (99.9 wt% purity Al and Al–0.5 wt% Sc) that are melted in an alumina crucible, stirred to ensure proper mixing, and poured into a graphite mold. The resulting alloys are coarse-grained with a typical grain size of 1–2 mm. TEM samples are prepared by cold-rolling the alloy into foils with a thickness of 350 μm. The foils are annealed in the primary single-phase region at 648°C in air for 24 h, quenched into cold water, and then aged in air at different temperatures, 300, 350, 400 or 450°C. The aging time is increased from 1 to 350 h to observe the nanoscale structural evolution. Discs of 3 mm diameter are punched from the foil, mechanically ground to 200 μm, and then jet electro-polished with a solution of 5% perchloric acid in methanol at −30°C. The precipitate sizes and morphologies are obtained from TEM observations.

CTEM is performed on a Hitachi 8100 operated at 200 kV. HREM is performed on a Hitachi HF2000-FEG microscope operated at 200 kV and a JEOL 4000EXII at 160 or 200 kV. A relatively low accelerating voltage (160 kV) was used for the samples oriented in the [110] direction to minimise radiation damage.

The precipitates are imaged using either centered

dark-field with a low-index superlattice reflection of the Al_3Sc phase or indirectly by strain-field contrast using a centered dark-field image by selecting a fundamental reflection. The number density is calculated from the number of precipitates per unit area divided by the thickness of the foil. The number of precipitates per unit area is evaluated with image-analysis software (NIH Image). The local thickness is calculated from the spacing of the Kossel–Möllenstadt fringes, which are produced within the disc of a convergent two-beam electron diffraction reflection (CBED).

The sizes of the smallest precipitates are determined by HREM. The accuracy for the precipitate size measurement is 0.4 nm, the interface being atomically sharp. Each average value of the precipitate radius is deduced from a measurement of more than 200 precipitates. Some of the HREM images are obtained by using a small objective aperture and selecting only the eight low-index superlattice reflections of the Al_3Sc phase. This technique allows a clearer view of the shape of the Al_3Sc/Al interface.

3. RESULTS

3.1. Morphology of Al_3Sc precipitates in an Al–0.3 wt% Sc alloy

The shape of an Al_3Sc precipitate is a function of size, and therefore of solute concentration, temperature, and aging time. By aging the Al–0.3 wt% Sc alloy at 300°C, precipitates with a very small size, that is less than 7 nm in diameter, are obtained. As seen in the HREM images in Fig. 2, faceted precipitates are observed for different aging times. After 6 h [Fig. 2(a)], faceting is not completely clear due to the small precipitate size (2 nm diameter). After 72 h [Fig. 2(b)], facets on the {100} and {110} planes are more visible. Increasing the aging temperature to 350°C increases the average precipitate size to 6 nm diameter. After 350 h [Fig. 2(c)], faceting on the {100} and {110} planes is unambiguous. Fig. 2(c) was taken using a small aperture to select the superlattice reflections of the Al_3Sc phase. When aged at 350°C for 24 h, Fig. 3, the same alloy exhibits slightly larger precipitates, that is more than 9 nm in diameter. These precipitates are also clearly faceted on the {100}, {110} and {111} planes. The {100} projection shows {100} and possibly {110} facets [Fig. 3(a)], while the {110} projection shows {100}, {110} and {111} facets [Fig. 3(b)].

When the temperature is increased to 400°C, the main faceting on the {100} planes tends to disappear at the expense of {110} planes, as shown in the HREM micrograph displayed in Fig. 4. The mean precipitate radius is 5 nm. At this same aging temperature, i.e. 400°C, larger precipitates (40 nm diameter), obtained after long aging times, form cuboids with the main facets on the {100} planes, as observed by CTEM in Fig. 5. No interfacial misfit dislocations could be observed, thereby supporting the hypothesis of perfect coherency between the Al and Al_3Sc phases for small precipitates.

3.2. Morphology of Al_3Sc precipitates in an Al–0.1 wt% Sc alloy

HREM observations of this alloy revealed completely different morphological features. In the Al–0.1 wt% Sc alloy aged at 300°C for 72 h, the observed irregular shapes suggest an unstable growth of the precipitates. As seen in Fig. 6, the precipitate shape exhibits lobes and cusps without an obviously favored crystallographic orientation. Nucleation in this alloy mainly occurs heterogeneously at dislocations. After aging at 350°C, the precipitate spatial distribution is highly non-uniform, with both isolated precipitates and arrays of precipitates. At short aging times, some of the isolated precipitates have cusps with an overall cubic shape. Their sizes range from 10 to 55 nm. After aging for more than 24 h at 350°C, the shape of the isolated precipitates tends to be even more concave. For some of these precipitates, the cusps are more pronounced indicating splitting of the precipitate (Figs 7 and 8). The precipitates, however, which are organized in arrays, are cuboidal (Fig. 9). For long aging times (130 h at 350°C), rod-like precipitates can also be seen as shown in Fig. 9. The Al_3Sc rods appear to be connected to larger cuboidal precipitates. The rod-like shape in opposition to a plate-like shape was confirmed by tilting experiments.

3.3. Coarsening behavior of Al_3Sc precipitates

Because of the complexity of the morphologies in the Al–0.1 wt% Sc alloy (Figs. 6–9), the coarsening kinetics of the Al_3Sc precipitates are only determined in the Al–0.3 wt% Sc alloy, where the precipitate morphology is more uniform. The change in the mean value of the precipitate radius, $<r>$, is measured for four different aging temperatures, 300, 350, 400 and 450°C. For a given aging temperature, the mean precipitate radius increases with increasing aging time. The results are presented in Fig. 10, where the mean precipitate radius is plotted versus the cube root of the aging time. As the mean precipitate radius increases, the number density of precipitates also decreases.

The slopes of the fitted lines for each temperature demonstrate an accelerating coarsening kinetics with increasing temperature. Loss of coherency, detected from the presence of interfacial dislocations (Fig. 11), is also observed when the precipitate size reaches about 40 nm in diameter.

Aging at high temperatures (above 350°C), and therefore small Sc supersaturations, produces heterogeneously nucleated precipitates. Arrays of Al_3Sc precipitates, nucleated along dislocation lines, are observed in the Al–0.3 wt% Sc alloy when aged above 350°C. The weak-beam dark-field image [Fig. 12(a)] shows clearly the dislocations on which the precipitates had been heterogeneously nucleated. In

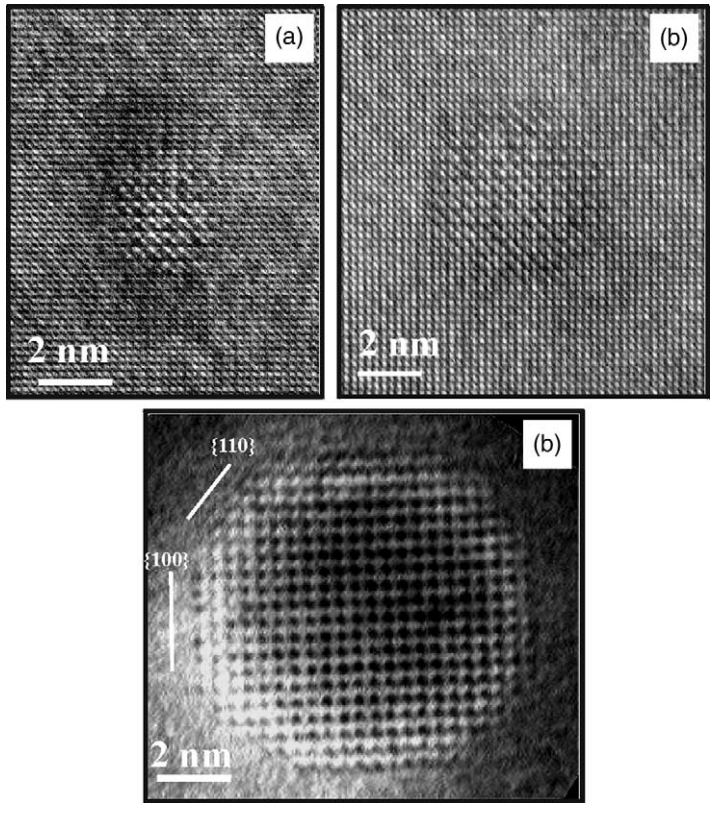

Fig. 2. HREM images of Al_3Sc precipitates after aging the Al–0.3 wt% Sc alloy at 300°C: (a) 6 h; (b) 72 h; and (c) 350 h. All the images were taken along the [100] zone axis.

Fig. 12(b), a bright-field image shows arrays of precipitates with coherency contrast.

An increasing Sc concentration leads to smaller precipitate sizes and to larger number densities, as shown in Table 1. After aging at 300°C for 72 h, the number density varies from $(5\pm2)\times10^{20}$ to $(4\pm2)\times10^{22}$ ppts/m^3 for the three Al(Sc) alloys (Table 1), which is in good agreement with Hyland's previous results on the homogeneous nucleation of Al_3Sc precipitates at 288 and 343°C in an Al–0.25 wt% Sc alloy. The effect of scandium concentration on the coarsening kinetics is, however, not reported in his article [10]. Assuming a cubic shape, the volume fraction of the Al_3Sc phase is obtained by multiplying the mean precipitate volume by the number density (Table 1) and is 3×10^{-3}, which is less than the value calculated from the lever rule, 7.06×10^{-3} (Table 3); the latter calculation requires an extrapolation of the extant solvus curve data from 375 to 300°C.

4. DISCUSSION

4.1. Morphology of Al_3Sc precipitate in an Al–0.3 wt% Sc alloy

The equilibrium shape of a precipitate is determined by minimizing the sum of the interfacial and the elastic energies at constant volume. The relative importance of the interfacial and elastic strain energies can be evaluated, however, through the L parameter introduced by Thompson *et al.* [18], which is used to represent the energy state of a precipitate at equilibrium. It is given by,

$$L = \frac{\varepsilon^2 C_{44} l}{\gamma}; \tag{1}$$

where $\varepsilon = 0.0125$ is the misfit strain, $C_{44} = 28.5$ GPa is an elastic constant of the matrix, and $l = 5$ nm is the measured precipitate dimension. The Thompson *et al.* model [18] assumes that the matrix and precipitate have the same elastic constants, which is not the case for the Al/Al_3Sc system (see Table 2). Nevertheless, using these values, L is of the order of 10^{-1}, suggesting that the interfacial energy alone controls the precipitate morphology.

The equilibrium shape of the Al_3Sc precipitates dictated by values of interfacial energies can be deduced from Wulff plots [22] using values found in the literature. Hyland *et al.* [23] calculated, using Embedded Atom Method (EAM) potentials, 33, 51 and 78 mJ/m^2 for the energies at 0 K of the {100}, {110} and {111} interfaces, respectively. Using these interfacial energies, a Wulff construction shows that the small Al_3Sc precipitates should be cubic with {100} facets. More recently, Asta *et al.* [24], using first-principles calculations, obtained larger values of

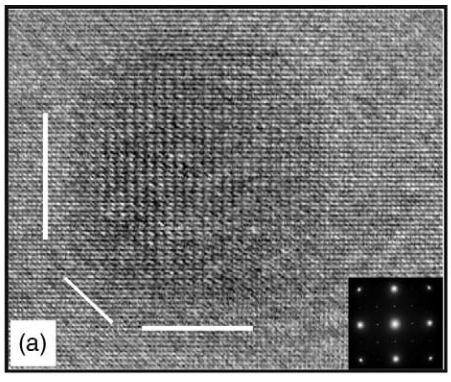

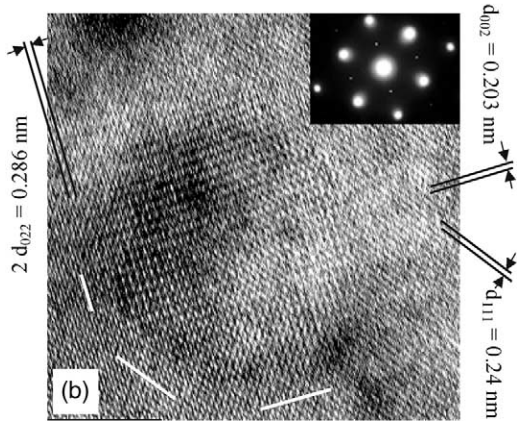

Fig. 3. HREM images of Al_3Sc precipitates obtained by aging the Al–0.3 wt% Sc alloy at 350°C for 24 h: (a) [100] zone axis; and (b) [110] zone axis.

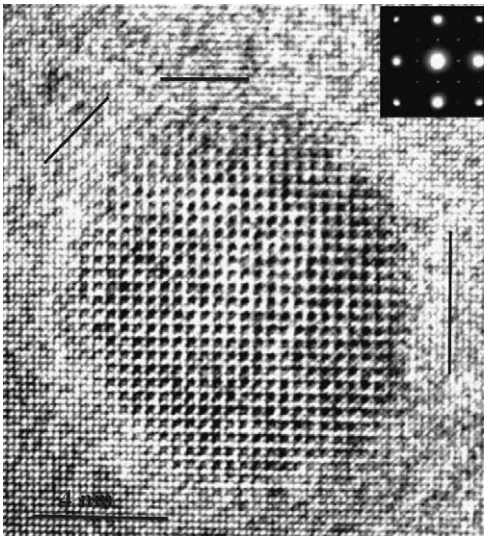

Fig. 4. HREM image of an Al_3Sc precipitate obtained by aging the Al–0.3 wt% Sc at 400°C for 1 h: taken along the [100] zone axis.

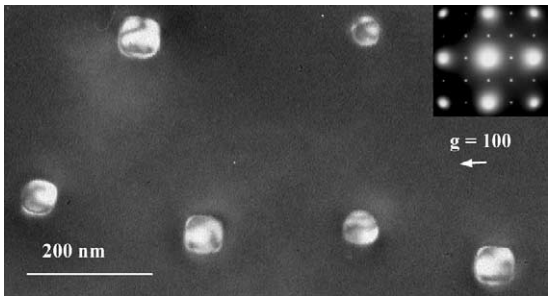

Fig. 5. Dark-field image of Al_3Sc precipitates in the Al–0.3 wt% Sc aged at 400°C for 120 h: [001] projection.

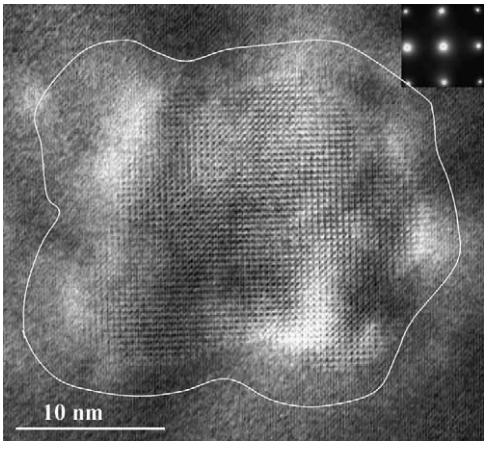

Fig. 6. HREM image of Al_3Sc precipitates in the Al–0.1 wt% Sc aged at 300°C for 72 h; taken along the [100] zone axis.

the interfacial energies; they are 192 mJ/m^2 for the {100} planes and 226 mJ/m^2 for the {111} planes at 0 K. They also concluded that the temperature dependence of the {111} interfacial energy is important, while the {100} interfacial energy varies weakly with temperature. According to these results, the Al_3Sc precipitates should exhibit facets on the {100}, {110} and {111} planes and these facets should become less distinct as temperature increases. Using their values at 0 K and 226 mJ/m^2 for the energy of the {110} interface [25], Wulff plots (Fig. 13) are constructed to visualize the observed morphologies. The equilibrium Wulff shape consists of 6 {100} planes (cube), 12 {110} planes (rhombic dodecahedron), and 8 {111} planes (octahedron). This shape is one of the regular Archimedean solids and is called a Great Rhombicuboctahedron.

Both the [100] and [110] projections of the precipitates reproduce the experimentally observed shape of the Al_3Sc precipitates [Figs 13(b) and (c)]. The {100} facets are the dominant ones in both the [100] and [110] views. The [110] projections exhibit similar {111} facets and the small {110} facets can be distinguished in both orientations (Fig. 3). Our HREM observations of the precipitate morphology and the ratio of the interfacial energies calculated by Asta *et al.* [25] therefore concur. The effect of temperature on precipitate morphology shown in Fig. 4 also agrees qualitatively with their conclusions. The morphology changes observed by comparing Figs 2, 4 and 5 also suggest an effect of the precipitate size.

The difficulty in seeing the facets with HREM on

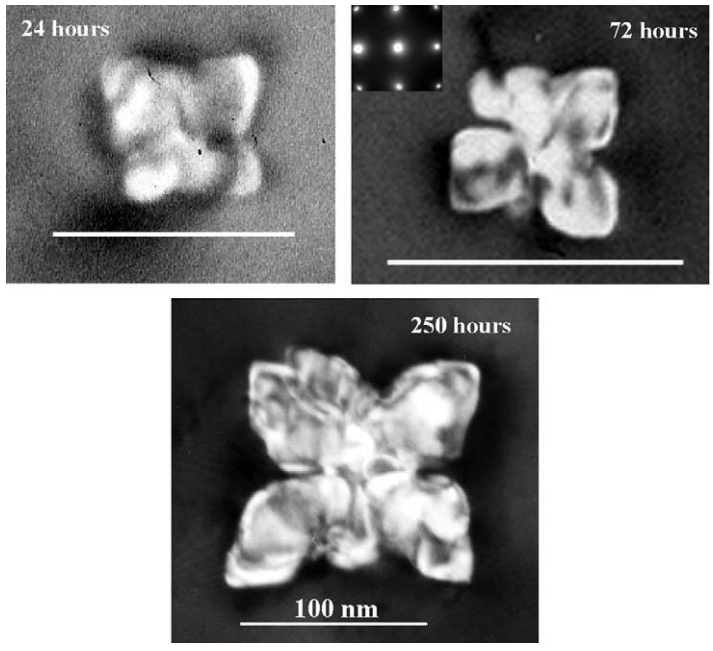

Fig. 7. Evolution of Al_3Sc precipitates in the Al–0.1 wt% Sc alloy aged at 350°C for 24, 72 and 250 h: all pictures are taken along the [100] zone axis. The scale bars represent 100 nm.

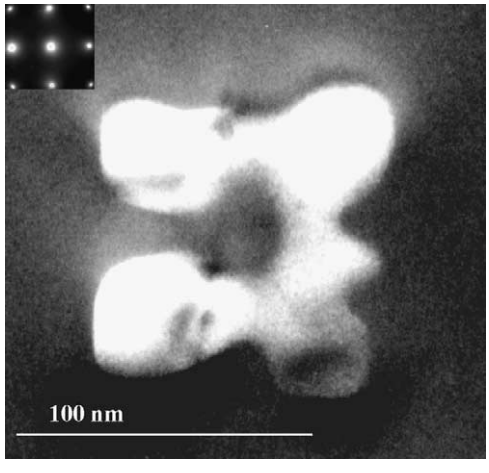

Fig. 8. Al_3Sc precipitate in the Al–0.1 wt% Sc alloy aged at 350°C for 145 h: [100] projection.

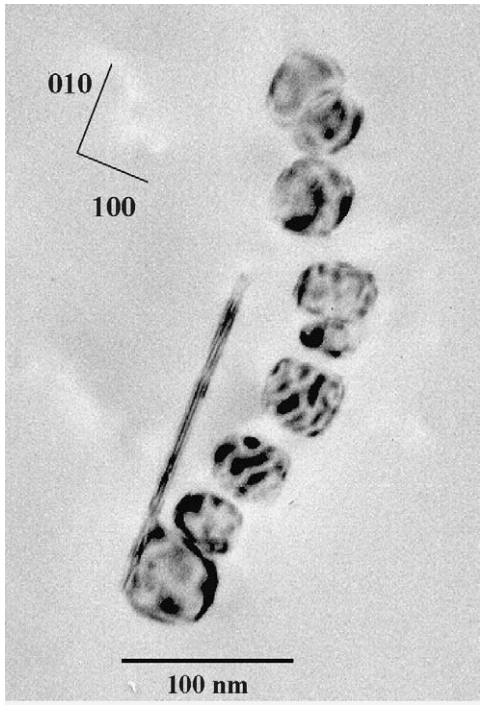

Fig. 9. Rod-like Al_3Sc precipitate and array of cuboidal precipitates in the Al–0.1 wt% Sc aged at 350°C for 130 h: [100] zone axis.

the smaller precipitates [Fig. 2(a)] may correspond to an intermediate stage before the equilibrium morphology is achieved. The relatively low aging temperature, 300°C, and therefore the low diffusivity of Sc in Al_3Sc, could explain why equilibrium has not been achieved for the shortest aging times; faceting is, however, clearly apparent after longer aging times [Figs 2(c) and 5].

4.2. Morphology of Al_3Sc precipitate in an Al–0.1 wt% Sc alloy

The smaller supersaturation in the Al–0.1 wt% Sc alloy causes growth instabilities during the growth of the Al_3Sc precipitates. The number density of nucleated precipitates may be low enough for the precipitates to grow in a supersaturated matrix before their diffusion fields commence overlapping. The morphology is then determined by the growth conditions rather than the equilibrium conditions. Similar observations were made for Al–Li alloys aged at

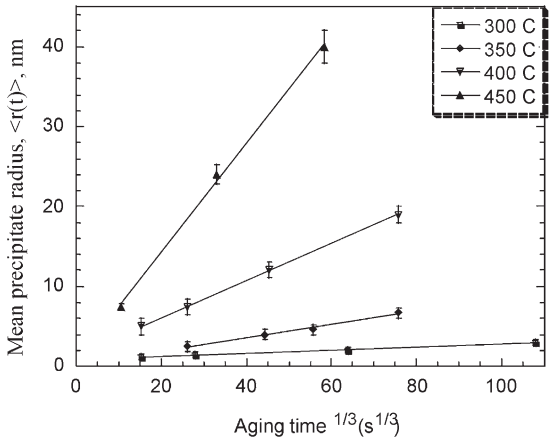

Fig. 10. Average precipitate radius (nm) as function of the cube root of the aging time and temperature.

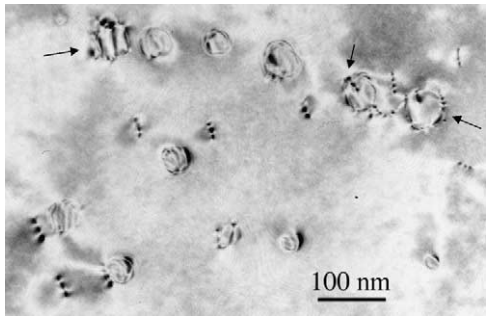

Fig. 11. Two-beam bright-field TEM micrograph of interfacial dislocations at Al_3Sc precipitates in Al–0.3 wt% Sc alloy aged at 400°C for 120 h: **g**=[200].

small supersaturations [21]. The further evolution of the shape of the large Al_3Sc precipitates exhibits a preferred orientation on the {100} planes, which can be related to the elastic anisotropy of the matrix (Table 2). The <100> directions are the soft directions of the aluminum matrix, while the <110> directions are the soft directions of the Al_3Sc precipitates [26]. This phenomenon has been discussed by Lee [27]. His two-dimensional Monte Carlo simulations demonstrates that the inverse anisotropy of the elastic constants of the matrix and the precipitate phase leads to a two- or four-fold symmetrical shape of precipitates, with possible splitting along the {100} planes as shown in Fig. 14. These results are in qualitative agreement with the observed Al_3Sc shapes exhibited in Figs 7 and 8. The morphologies obtained in this alloy are clearly complicated. The evolution from the shapes observed in Fig. 6 to the rod-like shapes (Fig. 9) or to the splitting shapes (Figs 7 and 8) remains to be explained in detail. The arrays of precipitates do not seem to undergo the splitting transformation, which also suggests that elastic interactions between these closely spaced precipitates are playing a role.

4.3. Coarsening behavior of an Al–0.3 wt% Sc alloy

According to Hyland's results on nucleation of Al_3Sc precipitates in an Al–0.25 wt% Sc alloy [10], the precipitate number density decreases as early as approximately 8000 s at 288°C, and after 1000 s at 343°C. Therefore, it is reasonable to assume that the Al_3Sc precipitates in our Al–0.3 wt% Sc alloy are in the coarsening stage when aged between 300 and 450°C for times greater than 1–2 h. Assuming that the precipitate shape can be approximated by a sphere

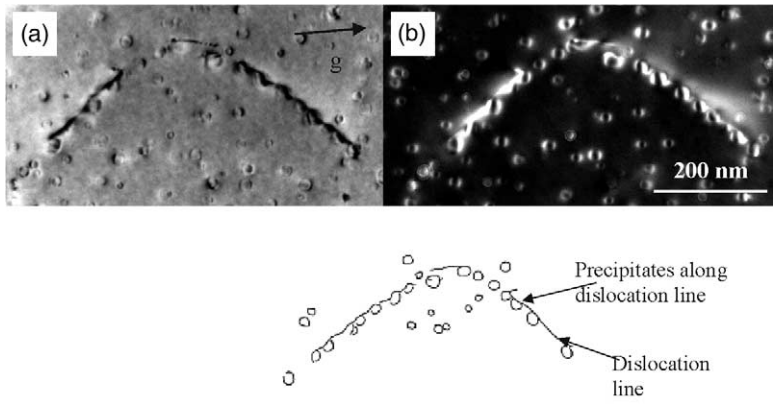

Fig. 12. Weak-beam dark-field (a) and bright field (b) images of Al–0.3 wt% Sc alloy aged at 350°C for 120 h: **g**=[200].

Table 1. Mean precipitate radius, $<r(t)>$, and number density after aging three different Al–Sc alloys at 300°C for 72 h

Alloy	Al–0.1 wt% Sc	Al–0.2 wt% Sc	Al–0.3 wt% Sc
Mean precipitate radius (nm), $\langle r(t)\rangle$	8.8±0.5	3.0±0.4	2±0.4
Number density (ppt/m^3)	(5±2)×10^{20}	(9±2)×10^{21}	(4±2)×10^{22}

Table 2. Elastic constants for pure aluminum and Al_3Sc phase [26]

	C_{11}[a]	C_{12}[a]	C_{44}[a]	E[b]	G[c]	A[d]
Al	108	61.3	28.5	70.7	26.3	1.21
Al_3Sc	189	43	66	164	68	0.9

[a] Elastic constants (GPa).
[b] Young modulus (GPa).
[c] Shear modulus (GPa).
[d] Zener anisotropy factor (dimensionless).

Table 3. Solid-solubility of Sc in primary α-phase (c_α), volume fraction of the Al_3Sc phase, Sc supersaturation, calculated and measured coarsening factors (k) for the Al–0.3 wt% Sc alloy, and the measured pre-exponential factor, D_o, of the Sc diffusivity for four different temperatures

	300°C	350°C	400°C	450°C
Solid-solubility (c_α) (at.% Sc)[a]	1.3564×10^{-3}	3.822×10^{-3}	9.552×10^{-3}	2.075×10^{-2}
Volume fraction of Al_3Sc phase[b]	7.06×10^{-3}	6.96×10^{-3}	6.74×10^{-3}	6.39×10^{-3}
Sc supersaturation (at.%)	0.179	0.176	0.171	0.159
Calculated k (m^3/s)	7.6×10^{-33}	3.7×10^{-31}	1.0×10^{-29}	1.7×10^{-28}
Measured k (m^3/s)	$(2.0\pm0.4)\times10^{-32}$	$(6.89\pm1.1)\times10^{-31}$	$(1.56\pm0.12)\times10^{-29}$	$(3.19\pm0.34)\times10^{-28}$
$\zeta = \frac{\text{measured } k}{\text{calculated } k}$	2.65	1.86	1.55	1.85
Measured pre-exponential factor, D_o (m^2/s)	2.0×10^{-4}	1.7×10^{-4}	1.6×10^{-4}	2.1×10^{-4}

[a] Calculated from the measured solid-solubility equation for Sc in the primary α-solid solution: $c_\alpha = \exp(\Delta S/R)\exp(-\Delta H/RT)$, where ΔS is the entropy change ($\Delta S/R = 6.57$) and ΔH is the enthalpy change (62.8 kJ mol^{-1}) for dissolving Sc in the α-phase [31].
[b] Calculated from the Al–Sc phase diagram using the lever rule.

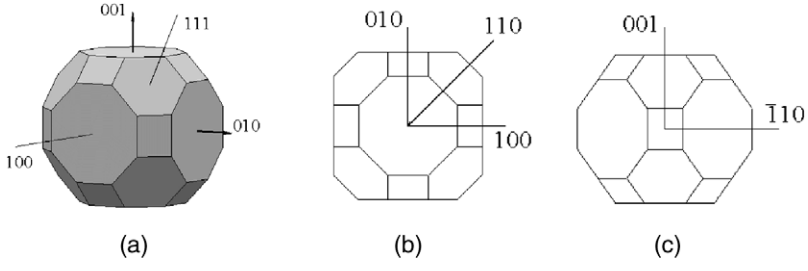

Fig. 13. Wulff's construction of the Al_3Sc precipitate morphology at 0 K based on first-principles values of the {100}, {110} and {111} interfacial energies: (a) three dimensional precipitate; (b) [100] projection; and (c) [110] projection.

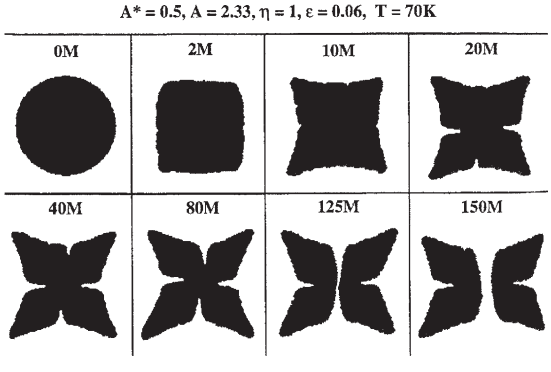

Fig. 14. Splitting of a coherent precipitate in an incommensurate anisotropic system [27]: A^* and A are the Zener anisotropy factors of the precipitate and the matrix, η is the ratio of the precipitate bulk modulus to that of the matrix, ε is the misfit parameter, and T is the absolute temperature. The numbers 2M, 10M, etc., refer to the number of Monte Carlo steps.

and the mean precipitate radius follows the Lifshitz–Slyozov–Wagner theory [28, 29] then the relevant equation is given by [28, 29]:

$$\langle r(t)\rangle^3 - \langle r_0(t)\rangle^3 = kt; \tag{2}$$

where k is a constant, and $\langle r(t)\rangle$ is the mean precipitate radius at time t.

A theoretical value of k, for an ideal solid-solution, is given by the following equation [30]:

$$k = \frac{8c_\alpha(1-c_\alpha)\gamma D V_m}{9RT(c_\beta - c_\alpha)^2} \tag{3}$$

where c_α is the solid solubility of Sc in Al deduced from solvus measurements obtained by Jo and Fujikawa [31, 32]; $c_\beta = 0.25$ at. fr. is the solubility of Sc in the stoichiometric Al_3Sc phase; $V_m = 1.035\times10^{-5}$ m^3/mol is the average atomic vol-

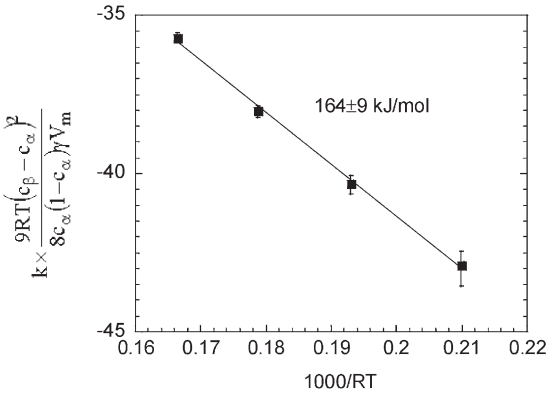

Fig. 15. Equation (3) is used to obtain the activation energy for coarsening in the Al–0.3 wt% Sc alloy.

ume per mol (V_m) of the Al_3Sc phase, deduced from $V_m = N_a a^3/4$ (N_a is Avogadro's number, $a = 0.4196$ nm is the lattice parameter of Al_3Sc); $D = 5.31\times10^{-4}\exp(-173\text{ kJ mol}^{-1}/RT)\text{ m}^2\text{s}^{-1}$ is the tracer diffusion coefficient of Sc in Al [33]; $\gamma \approx 200$ mJ/m^2 is an approximate average interfacial energy for the {100}, {110} and {111} planes [24].

Experimental values of k are determined from a plot of the cube of the precipitate radius versus the aging time. For plotting purposes, Fig. 10 shows the precipitate radius versus the cube root of the aging time; the exponent of t is 1/3 in agreement with LSW theory. Table 3 gives the scandium solubility for each temperature and compares the experimental values with the calculated values of k, showing a reasonably good agreement between the two sets of values (see ζ values in Table 3). The value of k obtained at 350°C also agrees with the results obtained by Novotny and Ardell [14]. Jo and Fujikawa were probably the first persons to conclude that the coarsening behavior was consistent with LSW theory [31]; however, the different data analyses do not permit a straightforward comparison of our results with their k values. The activation energy for diffusion, deduced from Fig. 15 using equation (3), 164±9 kJ/mol, and the activation energy for tracer diffusion of scandium in aluminum, 173 kJ/mol [33], agree within the experimental uncertainties. The activation energy for Sc diffusion in Al calculated from first principles is 154 kJ/mol [25], which is also in agreement with our experimental value (see Table 4). The average value of the pre-exponential factor D_o ($1.9\pm0.5\times10^{-4}$ m^2/s) is in reasonable agreement with the tracer value, 5.31×10^{-4} m^2/s [33].

Even though the mean radius of the Al_3Sc precipitates is proportional to the cube root of the aging time, proving agreement with the LSW theory in detail is complex. The theoretical distributions of precipitate size are obtained from the LSW theory and a modified LSW equation taking into account the precipitate volume fraction [34]. They are compared to our experimental size distributions in Fig. 16, which exhibit a reasonable fit between the LSW distributions and our experimental results. The effect of volume fraction on the coarsening kinetics is negligible in the Al–0.3 wt% Sc alloy [35, 36]. Although the Al(Sc) system is almost theoretically a model system to study precipitate coarsening (low volume fraction of the Al_3Sc phase and small solid-solubility of Sc in the α primary solid-solution), a complete study of coarsening behavior in this system remains a complicated and challenging problem.

The decreasing number density of precipitates with increasing aging temperature reflects the decreasing nucleation current with decreasing supersaturation. From classical nucleation theory, the nucleation current J (number of nuclei per unit time per unit volume) is [37]

$$J^* \propto ND \exp\left(-\frac{\Delta G^*}{RT}\right); \tag{4}$$

where N is the number of atomic nucleation sites per unit volume for homogeneous nucleation (or the number of sites at dislocation lines per unit volume for heterogeneous nucleation), ΔG^* is the nucleation barrier (which is inversely proportional to the square of the volume free energy change ΔG_v, for the formation of a critical size nucleus). Assuming an ideal solid-solution, ΔG_v is proportional to the logarithm of the supersaturation. The supersaturation is equal to the difference between the overall Sc concentration and the solid-solubility, c_α, at each aging temperature; values are given in Table 3 for the Al–0.3 wt% Sc alloy.

Reducing the Sc supersaturation by increasing the aging temperature at constant scandium concentration, appears to favor heterogeneous nucleation of precipitates at dislocations in the Al(Sc) system. In the case of coherent precipitation, dislocations can reduce the contribution of the lattice strain energy and, therefore, lower the activation energy barrier for nucleation [38, 39]. The reversible work for heterogeneous nucleation at dislocations is to a first

Table 4. Pertinent values for the diffusivity of scandium in aluminum

	Values	Techniques	References
Activation energy for Sc diffusion in Al	174	Tracer diffusivity	[33]
(kJ/mol)	154	First-principles calculations	[25]
	164±9	Precipitate coarsening	This work
Pre-exponential factor (m^2/s)	5.31×10^{-4}	Tracer diffusivity	[33]
	$(1.9\pm0.5)\times10^{-4}$	Precipitate coarsening	This work

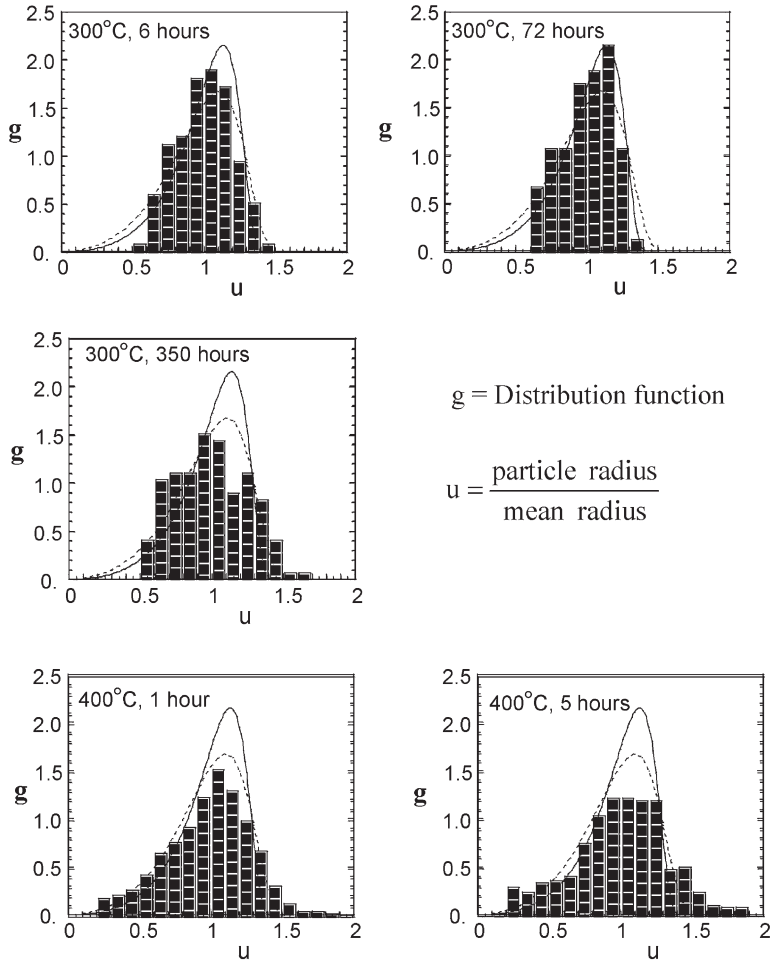

Fig. 16. Precipitate size distribution functions, g, as measured and as predicted (LSW and modified LSW theory, full and dashed lines respectively) versus normalized particle radius, u (ratio of precipitate radius to the mean precipitate radius), after aging at 300°C for 6, 72 and 350 h (HREM analysis) and at 400°C for 1 and 5 h (CTEM analysis).

approximation given by the contribution of the interfacial energy of the Al_3Sc precipitate and its volume free energy change; the strain energy being released by the destruction of dislocation line [39, 40]. The Al/Al_3Sc lattice misfit being positive, the precipitates are expected to nucleate in the tensile regions of an edge dislocation.

Coherency loss usually occurs when the precipitate size is large enough so that its scale is of the order of

$$n = \frac{1}{\delta}; \tag{5}$$

where n is the number of atomic planes in the aluminum phase coming into the Al/Al_3Sc interface, and δ, the lattice parameter misfit, is equal to 0.0125. Equation (5) yields $n = 80$ planes. The spacing between {200} planes is approximately 0.2 nm, so that the spacing between the misfit dislocations is approximately 16 nm. This value is in agreement with the observed misfit dislocations for a precipitate radius greater than 20 nm while 5 nm size precipitates are coherent (HREM).

5. SUMMARY AND CONCLUSIONS

We observed and discussed the following results.

- The exact morphology of the Al_3Sc precipitates was observed for the first time, with HREM, in an Al–0.3 wt% Sc alloy. The equilibrium shape of Al_3Sc precipitates obtained at 300°C is one of the regular Archimedean solids, a Great Rhombicuboctahedron, which has a total of 26 facets on the {100} (cube), {110} (rhombic dodecahedron) and {111} (octahedron) planes (Figs 2, 3 and 13). This morphology had been predicted by first-principles calculations of the {100}, {110} and {111} interfacial energies [24, 25].
- The effect of scandium content on nucleation and on the precipitate morphology was observed through the morphological evolution of Al_3Sc pre-

cipitates as a function of annealing time and temperature. The number density of precipitates increases with increasing scandium concentration at constant annealing temperature, that is with increasing supersaturation (Table 1). Equilibrium shapes are found in the Al–0.3 wt% Sc alloy (Figs 2 and 3), while non-equilibrium shapes are observed in the Al–0.1 wt% Sc alloy (Fig. 6).

- With increasing annealing temperature and therefore decreasing supersaturation, at constant Sc concentration, heterogeneous nucleation of Al_3Sc precipitates occurs at dislocations (Fig. 12).
- The effect of elastic anisotropy on the shape of the larger precipitates was discussed in the case of the lowest scandium concentration alloy (0.1 wt% Sc). The elastic anisotropy is thought to be responsible for the development of {100} oriented morphologies and the splitting of the shapes of the precipitates (Figs 7, 8, 9 and 14).
- The observed time dependence ($t^{1/3}$) of the coarsening behavior at 300, 350, 400 and 450°C of the Al_3Sc precipitates agrees with the Lifshitz–Slyozov–Wagner theory of coarsening (Figs 10 and 15).
- The activation energy for diffusion of Sc in the Al matrix obtained from the coarsening experiments is 164±9 kJ/mol, which agrees favorably with the activation energy obtained from tracer diffusion measurements of Sc in Al, 173 kJ/mol [33], and the value calculated from first principles, 154 kJ/mol [25] (Table 4). This implies that the diffusion of scandium in the aluminum matrix is the rate controlling step for the coarsening of the Al_3Sc precipitates, which in turn implies an evaporation–condensation mechanism for coarsening (Tables 3 and 4 and Fig. 15).

Acknowledgements—This research is supported by the United States Department of Energy, Basic Sciences Division, under contract DE-FG02-98ER45721. We would like to thank Professors Mark D. Asta, David C. Dunand, and Peter W. Voorhees (Northwestern University) for interesting and useful discussions, Professor Asta for permission to quote his unpublished results, Dr Joanne L. Murray (Alcoa Research Laboratory) for telling us the correct name (Great Rhombicuboctahedron) for the observed morphology, Argonne National Laboratories and especially Dr Roseann Csencsits for use of the JEOL4000EXII. We would also like to thank Ashurst Inc. for supplying the Al–Sc master alloy, Dr Robert W. Hyland for useful discussions of the physical metallurgy of Al–Sc alloys, and Professor Alan J. Ardell for a preprint of his paper. Fig. 14 is courtesy of Professor Jong K. Lee.

REFERENCES

1. Toporova, L. S., Eskin, D. G., Kharakterova, M. L. and Dobatkina, T. B., *Advanced Aluminum Alloys Containing Scandium*. Gordon, 1998.
2. Sawtell, R. R. and Jensen, C. L., *Metall. Trans.*, 1990, **21A**, 421.
3. Sawtell, R. R., Ph.D. thesis, University of California at Berkeley, 1988.
4. Bradley, E. L., Ph.D. thesis, University of California at Berkeley, 1990.
5. JCPDS-International Centre for Diffraction Data, v. 2.00, 1998.
6. Elliot, R. P. and Shunk, F. A., *Bull. Alloy Phase Diag.*, 1981, **2**(2).
7. Bradley, E. L., Emigh, R. A. and Morris, J. W. Jr, *Scripta metall. mater.*, 1991, **25**, 717.
8. Fuller, C. B., Seidman, D. N. and Dunand, D. C., *Scripta metall.*, 1999, **40**, 691.
9. Harada, Y. and Dunand, D. C., *Acta mater.*, 2000, **48**(13), 3477.
10. Hyland, R. W., *Metal. Trans. A*, 1992, **23**(7), 1947.
11. Murray, J. L., *J. Phase equilibria*, 1998, **19**(4), 380.
12. Sano, N., Hasegawa, Y. and Hono, K., *J. de Physique*, 1987, **C6**(48), 337.
13. Drits, M. Y., *Phys. Met. Metall.*, 1984, **57**(6), 118.
14. Novotny, G.M. and Ardell, A.J., *Mat. Sci. Eng. A*, 2001, to appear.
15. Ardell, A. J., *Acta metall.*, 1966, **14**, 1295.
16. Doi, M., *Mater. Sci. Engng*, 1985, **74**, 139.
17. Miyazaki, *Mater. Sci. Engng*, 1982, **54**, 9.
18. Thompson, M. E., Su, C. S. and Voorhees, P. W., *Acta mater.*, 1994, **42**(6), 2107.
19. Wang, Y. and Katchaturyan, A., *Phil. Mag. A*, 1995, **72**, 1161.
20. Katchaturyan, A. G., Semevskaya, S. V. and Morris, J. W. Jr, *Acta metall.*, 1988, **36**(6), 1563.
21. Baumann, S. F. and Williams, D. B., *Metall. Trans. A*, 1985, **16**, 1203.
22. Sutton, A. P. and Balluffi, R. W., *Interfaces in Crystalline Materials*. Oxford University Press, Oxford, 1996.
23. Hyland, R. W., Asta, M., Foiles, S. M. and Rohrer, C. L., *Acta mater.*, 1998, **46**(10), 3667.
24. Asta, M., Foiles, S. M. and Quong, A. A., *Phys. Rev. B.*, 1998, **57**, 11265.
25. Asta, M. and Ozolins, V., unpublished results.
26. Hyland, R. W. and Stiffler, R. C., *Scripta metall. mater.*, 1991, **25**(2), 473.
27. Lee, J. K., in *The 4th International Conference on Solid–Solid Phase Transformations*, ed. M. Koiwa. Japan Institute of Metals, 1999, p. 525.
28. Wagner, C., *Z. Elektrochem.*, 1961, **65**, 581.
29. Lifshitz, I. M. and Slyozov, V. V., *Phys. Chem. Solids*, 1961, **19**, 35.
30. Calderon, H. A., Voorhees, P. W., Murray, J. L. and Kostorz, G., *Acta metall. mater.*, 1994, **42**(3), 991.
31. Jo, H. H. and Fujikawa, S. I., *Mater. Sci. Engng*, 1993, **A171**, 151.
32. Fujikawa, S., Sugaya, M., Takei, H. and Hirano, K., *J. Less common metals*, 1979, **63**, 87.
33. Fujikawa, S. I., *Defect and Diffusion Forum*, 1997, **143-147**, 115.
34. Ardell, A. J., *Acta metall.*, 1872, **20**, 61.
35. Voorhees, P. W., *Annu. Rev. Mater. Sci.*, 1992, **22**, 197.
36. Che, D. Z., Spooner, S. and Hoyt, J. J., *Acta mater.*, 1997, **45**(3), 1167.
37. Aaronson, H. I., *Metall. Trans. A*, 1993, **24**, 241.
38. Nicholson, R. B., in *Phase Transformations*. 1968, p. 269; Martin, G., in *Solid State Phase Transformations in Metals and Alloys*, ed. D. de Fontaine (Les Editions de Physique, Orsay, France, 1978), pp. 337–406.
39. Cahn, J. W., *Acta metall.*, 1956, **4**, 449.
40. Cahn, J. W., *Acta metall.*, 1957, **5**, 168.